Compact Differential Diplex Filtenna with Common-Mode Suppression for Highly Integrated Radio Frequency Front-Ends

Dajiang Li, Ming-Chun Tang, Yang Wang, Kun-Zhi Hu, and Richard W. Ziolkowski

***Abstract* — A compact, differential diplex filtenna (DDF) with common mode (CM) suppression is presented. A rectangular dual-mode patch is developed that operates in both its TM_{10} mode and a reshaped TM_{30} mode to realize two passbands. Two capacitively loaded loop (CLL) resonators that work at different frequencies are combined with the dual-mode patch to enhance its operational bandwidth and to provide a second-order Chebyshev filter response for both passbands. A slot-coupled differential feed is adopted to suppress the harmonic and CM noise and to obtain symmetrical radiation patterns with low cross-polarization levels. The design process, which is based on filter synthesis theory, is detailed. A prototype operating over the 2.4G and 5.8G WLAN bands was fabricated, assembled, and tested. The measured results, in good agreement with their simulated values, confirm that it attains maximum broadside realized gains of 5.45 and 8.5 dBi, and –10-dB fractional impedance bandwidths of 2.4% (2.42–2.48 GHz) and 5.2% (5.65–5.95 GHz) for the lower and upper passbands, respectively. Moreover, it exhibits good out-of-band rejection levels of 18dB and 29dB for the lower and upper stopbands, respectively.**

***Index Terms* — Common-mode (CM) suppression, differential feed, diplex antennas, diplexers, filtennas**

I. Introduction

Filtennas [1]-[6] have become a popular means to attain a more compact system footprint. Similarly, diplexers have become one of the critical components in multi-band wireless communication systems [7]. They are used to separate their operating frequencies into the desired bands. Many efforts have developed different versions of diplex filtennas. They can be divided into two general classes, i.e., those based on substrate integrated waveguides (SIWs) [8]-[10], and on microstrip patch antennas [11]-[14]. For example, a SIW diplex filtenna was designed in [8] that employed a dual-mode SIW cavity which was modified with a ring slot. The compact diplex filtenna presented in [9] utilizes three horizontally-placed SIW cavities and concomitantly achieves an enhanced bandwidth. The compact vertically-integrated diplex filtenna developed in [10] used a common feed of two radiating SIW cavities. The high-isolation broadband diplex patch filtenna reported in [11] integrated two filters with a single patch antenna. Similarly, the diplex filtenna developed in [12] coupled a single patch with two sets of resonator-based filter channels. All of these diplex filtenna works focused on the realization of a small frequency ratio (FR), i.e., the ratio of the center frequency of the upper band to that of its lower one being less than 2.

On the other hand, diplex filtennas with large FRs were developed in [13], [14]. They met the requirements of many advanced wireless communication systems with operating bands having expansive ranges. For instance, the diplex filtenna developed in [13] cascaded a dual-band patch antenna and a microstrip diplexer composed of two bandpass filters. The diplex filtenna presented in [14] consisted of a dual-band patch integrated with two step-impedance resonators.

Another technology that has proven beneficial for RF front-ends is the differential feed. Compared to the single-ended antennas in [1]–[5] and [8]-[14], differentially-fed antennas are more suitable for integration with the differential circuits that have also become widely used [15]. Because there is no need for additional baluns or hybrid couplers, their structures are less complex, have lower losses and even lower costs. Moreover, differentially-fed antennas possess many advantageous performance characteristics including common-mode (CM) and harmonic suppression, symmetric radiation patterns, and low cross-polarization levels. Consequently, a differential diplex filtenna (DDF) with a high FR would have great practical significance in many application scenarios. This is particularly the case when the systems require more compact sizes, higher integration densities, and stronger anti-interference capabilities. Nevertheless, DDFs have rarely been reported to the best of our knowledge.

A compact DDF with good CM suppression is presented in this Communication for use in highly integrated RF front-ends. Because the developed filtenna exploits the TM_{10} and TM_{30} modes of the patch itself, the composite system achieves a large FR while remaining compact in size. A slot-coupled differential feed structure is developed to suppress the harmonic and CM noise and to obtain symmetrical radiation patterns and low cross-polarization levels. It will be further demonstrated that the developed DDF also has good out-of-band rejection performance characteristics. A prototype operating over the 2.4 G and 5.8 G WLAN bands was fabricated, assembled, and tested. It will be shown that the measured results are in good agreement with their simulated values.

II. Design of the Developed DDF

Fig. 1 shows the configuration of the developed DDF. Its optimized design parameters are given in Table I. The filtenna is realized with two copper-clad Rogers RO4003 substrates. Both have a relative dielectric constant of 3.55, a loss tangent of 0.0027, and a thickness of 0.813 mm. An air gap with height H_{air} between the two substrates is adopted to facilitate achieving a good impedance match. The filtenna consists of four parts: one slot-modified dual-mode rectangular radiation patch, one ground plane with two slots, two pairs of differential feedlines and two half-wavelength capacitively loaded loop (CLL) resonators, i.e., $L_4 + 2L_5 + 2L_6 \approx \lambda_{g1}/2$, $L_9 + 2L_{10} \approx \lambda_{g2}/2$, where λ_{g1} and λ_{g2} are the wavelengths in the substrate at the resonance frequencies of the CLL associated with Port 1 and Port 2, respectively.

Manuscript received on Dec. 08, 2020; revised on May 03, 2021; and accepted on May 07, 2021.

This work was supported in part by the National Natural Science Foundation of China contract number 61922018; in part by the Chongqing Natural Science Foundation contract number cstc2019jcyjjqX0004; and in part by the Australian Research Council grant number DP160102219. (*Corresponding author: Ming-Chun Tang.*)

D. Li, M. -C. Tang, Y. Wang, and K. -Z. Hu are with the Key Laboratory of Dependable Service Computing in Cyber Physical Society Ministry of Education, School of Microelectronics and Communication Engineering, Chongqing University, Chongqing 400044, China (E-mail: tangmingchun@cqu.edu.cn).

R. W. Ziolkowski is with the University of Technology Sydney, Global Big Data Technologies Centre, Ultimo NSW 2007, Australia (E-mail: richard.ziolkowski@uts.edu.au).

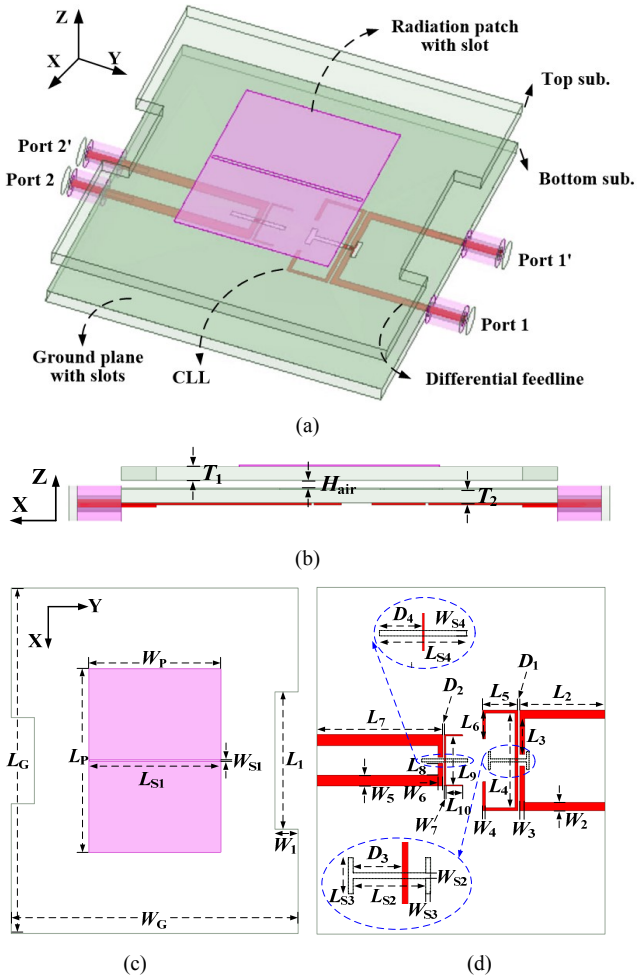

Fig. 1. The DDF configuration and its design parameters. (a) 3-D isometric view. (b) Side view. (c) Top view of the upper surface of the top substrate. (d) Top view of the lower surface of the bottom substrate.

TABLE I. OPTIMIZED DESIGN PARAMETERS OF THE DEVELOPED DDF (DIMENSIONS IN MILLIMETERS)

$L_1 = 24$	$L_2 = 14.8$	$L_3 = 7.2$	$L_4 = 17.4$	$L_5 = 6.1$
$L_6 = 5.0$	$L_7 = 21.8$	$L_8 = 2.5$	$L_9 = 8.5$	$L_{10} = 2.95$
$L_P = 34$	$L_G = 60$	$L_{S1} = 21.8$	$L_{S2} = 6.3$	$L_{S3} = 3.1$
$L_{S4} = 8.0$	$D_1 = 0.35$	$D_2 = 0.1$	$D_3 = 5.25$	$D_4 = 4.05$
$W_1 = 4.0$	$W_2 = 1.4$	$W_3 = 0.8$	$W_4 = 0.5$	$W_5 = 1.9$
$W_6 = 0.8$	$W_7 = 0.2$	$W_P = 23$	$W_G = 50$	$W_{S1} = 0.2$
$W_{S2} = 0.5$	$W_{S3} = 0.4$	$W_{S4} = 0.5$	H_{air}=0.5	NULL

The patch lies on the upper surface of the top substrate. The two frequency bands of the system correspond to the excitation of its TM_{10} and TM_{30} modes. A narrow rectangular slot is etched into it to help reshape the radiation pattern of its TM_{30} mode. The slot-loaded patch simultaneously acts as a radiating element and as the second-stage resonator of a second-order bandpass filter for both operating frequency bands. On the lower surface of the bottom substrate, there are two pairs of differential feedlines and two CLLs. The CLLs function as the corresponding first-stage resonators. An H-shaped slot and a rectangular slot are introduced into the common ground plane that lies on the upper surface of the bottom substrate to realize the coupling between the corresponding CLL resonators and the resonant modes of the patch radiator in the corresponding operational band. Thus, second-order bandpass filter responses are achieved for each band. Four 50-Ω coaxial connectors were selected to differentially feed the filtenna, two for each of its ports. When Port 1 (Port 2) is excited, the antenna operates in the lower (upper) band.

A. Dual-Mode Dual-Band Microstrip Patch Antenna

In order to obtain two different operating frequency bands yielding a large FR, the TM_{10} and TM_{30} modes of the differentially-fed rectangular microstrip patch antenna (MPA) shown in Fig. 2(a) are employed. Based on cavity-mode theory, the resonance frequencies, f_{mn}, of its TM_{mn} modes are expressed as:

$$f_{mn} = \frac{c}{2\sqrt{\varepsilon_{eff}}}\sqrt{\left(\frac{m}{L_P}\right)^2 + \left(\frac{n}{W_P}\right)^2} \quad (1)$$

where c represents the speed of light and ε_{eff} is the effective dielectric constant of the medium. The integers m and n are the mode indices along the x- and y-axis directions, respectively. The terms L_p and W_p are the length and width of the patch.

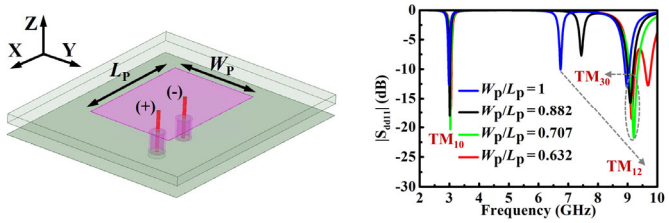

Fig. 2. Differentially-fed rectangular MPA. (a) Configuration. (b) Simulated differential mode (DM) $|S_{11}|$, i.e., $|S_{dd11}|$, values as a function of the source frequency as the ratio W_p / L_p varies by changing W_p while keeping L_p constant. $L_p = 34.0$ mm and $W_p = 21.5$ mm for the $W_p / L_p = 0.632$ case. The air gap has the height: $H_{air} = 0.5$ mm.

Because a differential mode (DM) feed is adopted, the even modes (TM_{20}, TM_{21}…..) are suppressed while the odd modes (TM_{10}, TM_{12}, TM_{30}…..) are retained [16]. Eq. (1) indicates that the TM_{12} mode would be shifted out of the frequency range between the TM_{10} and TM_{30} modes when $W_p < 0.707\ L_p$. Moreover, this choice prevents any redundant harmonic noise modes from being excited in that frequency range. The HFSS (high frequency structure simulator) results in Fig. 2(b) verify these features. However, the sidelobes in the E-plane (x-direction) of the radiation pattern of the TM_{30} mode theoretically are significantly high. This property definitely must be avoided if unidirectional radiated fields are desired.

B. Reshaping the Radiation Pattern of the TM_{30} Mode

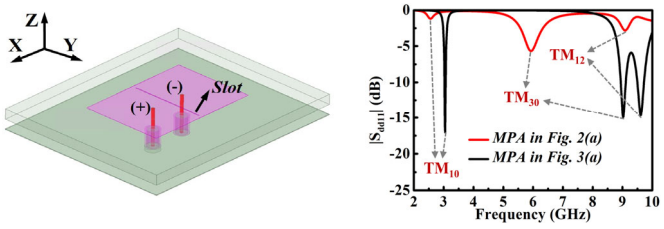

Fig. 3. MPA with the center slot. (a) Configuration. (b) Comparison of its simulated $|S_{dd11}|$ values with those of the MPA without the slot. The length and width of the narrow slot are 19.0 mm and 0.2 mm, respectively.

It is known that the sidelobe levels of the TM_{30} mode can be effectively reduced by loading the two principal radiation edges of the rectangular patch with slots [14]. Since this decrease in the sidelobe levels is typically achieved at the expense of reducing the area available for radiating fields, the realized gain is significantly smaller in the operating band. As an alternative, a non-resonant narrow rectangular slot can be etched on the center of the patch along the y-direction as shown in Fig. 3(a). This approach not only suppresses the sidelobes, but it also maintains high realized gain values. The simulated $|S_{dd11}|$ values of this slot-modified patch are compared in Fig. 3(b) with those of the MPA without the slot shown in Fig. 2(a). Note

that the FR becomes less than 3 mainly due to the presence of the slot. Our simulation studies show that the FR can be adjusted slightly, e.g., to 5.8G/2.45G or 5.2G/2.45G, by simply altering the rectangular slot length and the patch width. In order to clearly explain the sidelobe suppression mechanism, the surface current distributions and *E*-plane radiation patterns of the distinctly different TM_{30} modes of the MPAs without and with the slot are compared in Fig. 4.

It is well-known that an MPA can be viewed as a surface current radiator. The current distributions along the long *x*-directed edges primarily determine the associated *E*-plane radiation pattern. There are three half-wavelength periods of the electric field of the TM_{30} mode along the *x*-direction at its resonance frequency point. Fig. 4(a) shows the currents directions near both ends of the patch without the slot are opposite to those in its middle. This phase change of the currents causes the sidelobes shown in its *E*-plane radiation pattern, which is the standard TM_{30}-mode behavior. However, when the non-resonant narrow rectangular slot loads the patch, those out-of-phase currents are forced to circumnavigate it as shown in Fig. 4(b). It is clearly observed that the currents on the patch are then mainly divided into two parts which are uniformly aligned along the +*x*-direction. Therefore, the *E*-plane sidelobes of the TM_{30} mode of the MPA with the slot are significantly reduced, and, hence, its radiation gain is enhanced.

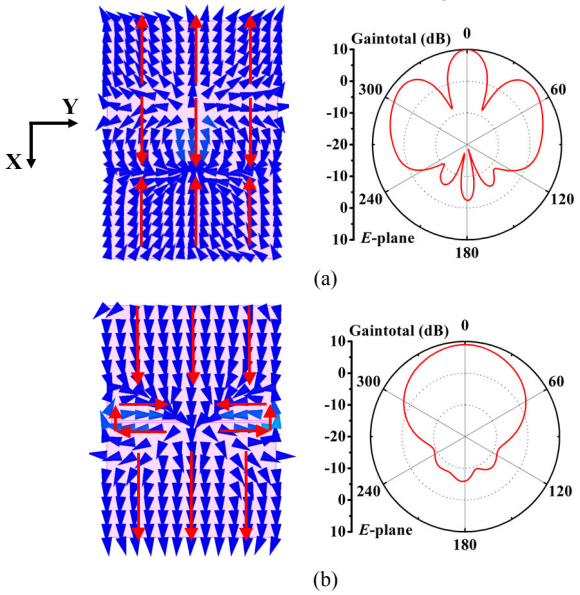

Fig. 4. Surface current distributions and *E*-plane radiation patterns of the TM_{30} mode of the rectangular MPA (a) without the slot and (b) with the slot at its resonance frequency.

C. Filter Analysis of the CLL Resonator Designs

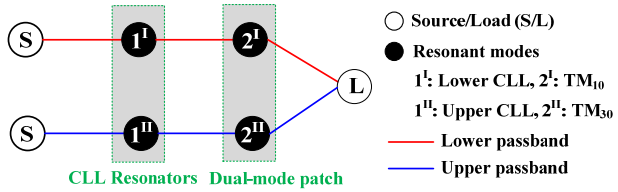

Fig. 5. Equivalent resonator-based topology of the developed DDF.

An electric wall along the center line of the CLL resonator is well formed with the DM excitation. One can then view the composite structure as a single-ended type [17]. Consequently, the actual DDF configuration shown in Fig. 1 can be represented as the equivalent coupled-resonator network shown in Fig. 5. The two CLL resonators and the patch with its two resonant modes are introduced to achieve the desired filter responses. The well-known filter synthesis theory based on the topology of a network [18] can then be used to guide the design of the filtenna.

Mutual couplings between the CLL resonators for the lower and upper passbands associated with the TM_{10} and TM_{30} modes of the patch resonator are realized, respectively, by an H-shaped slot and a rectangular slot etched on the ground plane as shown in Fig. 1. The coupling strength of each passband is flexible and adjusted by changing the length of the corresponding slot. When the two resonators are mutually coupled, two distinct resonance frequencies are observed in our full-wave simulation studies. The coupling coefficient can be extracted from them as [18]:

$$k = \frac{f_2^2 - f_1^2}{f_2^2 + f_1^2} \tag{2}$$

where f_1 and f_2 are, respectively, the resonance frequencies of the two coupled resonators when their ports are weakly-coupled. The design curves of the coupling coefficients, i.e., k^I and k^{II}, are both shown in Fig. 6. The values of k^I (k^{II}) increase as the slot length L_{S2} (L_{S4}) increases. The desired coupling coefficient values of two passbands can then be realized by tuning the parameters L_{S2} and L_{S4} of each corresponding slot, respectively.

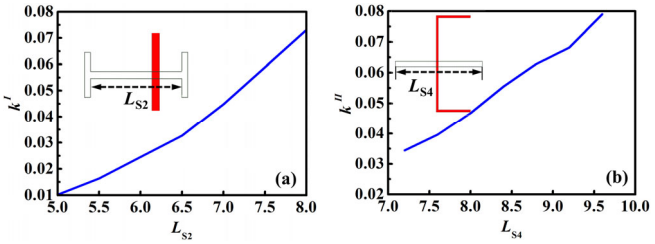

Fig. 6. Design curves of the two coupling coefficients for the lower and upper passbands. (a) k^I versus the slot length L_{S2}. (b) k^{II} versus the slot length L_{S4}.

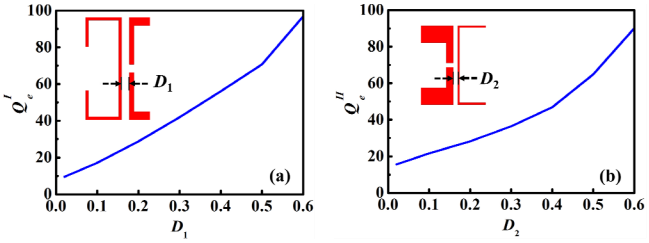

Fig. 7. Design curves of the two external quality factors for the lower and upper passbands. (a) Q_e^I versus D_1. (b) Q_e^{II} versus D_2.

The external quality factor Q_e with the input port represents the level of coupling between the differential feedline and the associated CLL resonator. The coupling strength is mainly controlled by the distance between the differential feedline and the CLL resonator. The value of Q_e is evaluated as [18]:

$$Q_e = \frac{2\pi f_0 \cdot \tau}{4} \tag{3}$$

where f_0 is the resonance frequency of the corresponding CLL resonator. The term τ is the group delay of the corresponding differential reflection coefficient. For the *i-th* port, τ_{ii} is calculated as:

$$\tau_{ii} = \frac{-deriv\left[ang\_deg(S_{ddii})\right]}{2\pi} \tag{4}$$

where *deriv[•]* represents the derivative with respect to the source frequency and *ang_deg (•)* represents the phase in degrees. The S_{ddii} values are obtained from the full-wave simulations under the condition that only the *i-th* CLL resonator is excited by its two differential ports [18]. With the coupling gap lengths of the lower and upper band CLL resonators being D_1 and D_2, respectively, Fig. 7 shows the extracted values of Q_e^I versus D_1 and Q_e^{II} versus D_2 calculated from (3). It can be seen that Q_e^I (Q_e^{II}) decreases as D_1 (D_2) increases. The desired external

quality factor values for the two passbands can then be achieved by adjusting the corresponding coupling gaps lengths.

Finally, it is desired that the two CLL-patch mode systems yield an overall second-order Chebyshev bandpass filter response for the high FR dual-band operation. The center frequency of the lower (upper) passband is desired to be located at 2.45 GHz (5.8GHz) with an impedance bandwidth of 2.9% (4.6%) and an in-band return loss no greater than 10 dB. The corresponding normalized coupling matrix that will synthesize these lower and upper passbands is deduced with relations in [18] as:

$$M^{I}=M^{II}=\begin{array}{c} \\ S \\ 1 \\ 2 \\ L \end{array}\begin{array}{c} \begin{array}{cccc} S & 1 & 2 & L \end{array} \\ \begin{bmatrix} 0 & 0.8575 & 0 & 0 \\ 0.8575 & 0 & 1.0201 & 0 \\ 0 & 1.0201 & 0 & 0.8575 \\ 0 & 0 & 0.8575 & 0 \end{bmatrix} \end{array} \tag{5}$$

The specific design parameters, i.e., the coupling coefficients k, and external quality factors Q_e, under DM operation that will yield the desired operational passbands can be calculated with well-known equations that utilize the components of the coupling matrix (5) [18]. As a result, $k^{I}=0.030$, $Q_e^{I}=46.9$, $k^{II}=0.047$, and $Q_e^{II}=29.6$. Therefore, the anticipated bandpass filtering responses of the two operational passbands are achieved by properly choosing the initial dimensions of the physical structure according to the design curves in Figs. 6 and 7 and then slightly optimizing the entire structure with numerical parameter studies.

III. Principles of the DM-based CM Suppression

To better understand the working principles of the CM suppression associated with the differential feed, the current distributions of the optimized DFF at 2.45 GHz (the center frequency of the lower passband) and 5.8 GHz (the center frequency of the upper passband) under different excitation mechanisms are presented in Fig. 8. When the filtenna is excited by signals having equal amplitudes and the same phases (CM excitation), as shown in Fig. 8(a), the lower passband CLL forms a virtual magnetic wall along the central plane normal to it. The currents on the two arms of the CLL flow in opposite directions. Thus, there is little vertical electrical field flowing through the slot on the ground [19], i.e., nearly no energy is transmitted to the patch via the coupling slot. Moreover, it is observed that the currents on the patch are very weak, indicating that the CM signals are strongly reflected. In contrast, under DM operation, the filtenna is excited by signals with equal amplitudes, but opposite phases. As shown in Fig. 8(b), an electrical wall is generated along the central normal plane of the lower passband CLL. The currents on both arms of this CLL are in the same direction. Consequently, energy is strongly magnetically coupled to the patch through the slot. Thus, the input DM signals are radiated effectively. Moreover, very weak currents are found on the upper passband CLL, i.e., excellent isolation between the two operating frequency bands is attained.

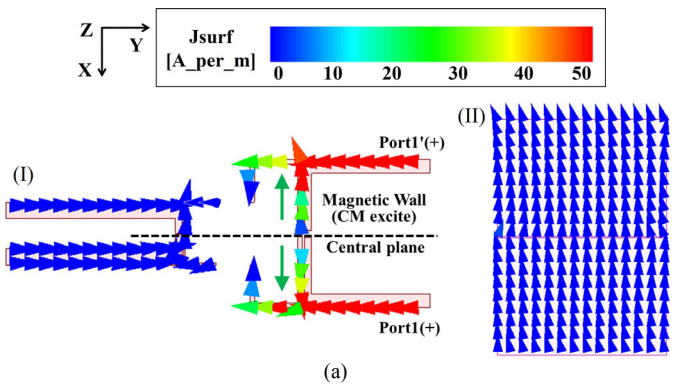

(a)

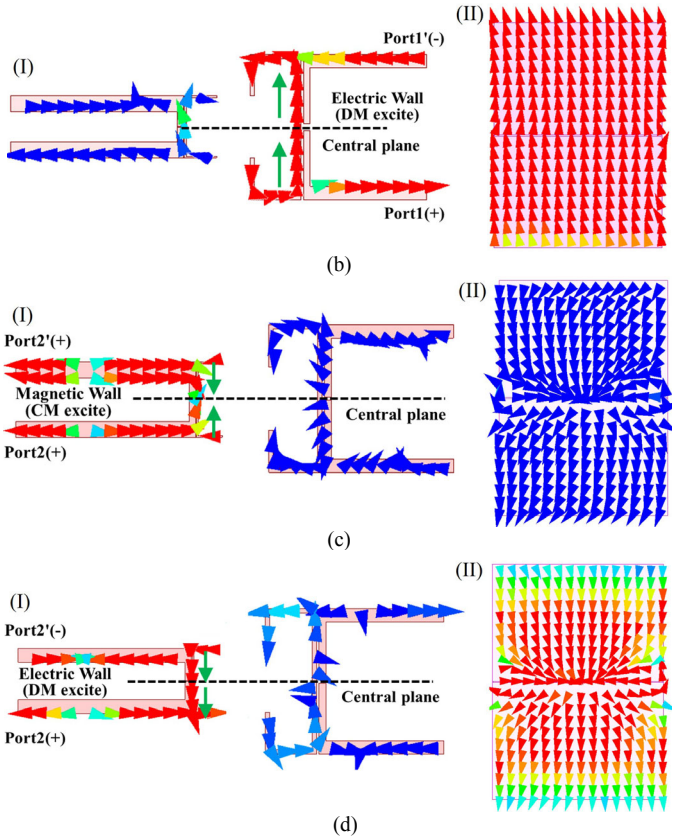

Fig. 8. Current distributions on the structures of the developed DDF: (I) differential feedlines and CLL resonators, and (II) radiation patch. (a) CM excitation and (b) DM excitation at 2.45 GHz. (c) CM excitation and (d) DM excitation at 5.8 GHz.

As noted in [20], the central normal plane of an MPA can be regarded as a virtual electric wall for all of the odd-order modes. Consequently, the TM_{10} and TM_{30} modes of the patch can be excited under DM operation and suppressed under CM operation. Therefore, the same CM and DM phenomena are found with the TM_{30} operation at 5.8 GHz. This outcome is illustrated in Figs. 8(c) and 8(d). Since the TM_{10} and TM_{30} modes dominate the radiation performance, respectively, of the lower and upper passbands, the DFF exhibits excellent CM rejection capabilities in both operating bands.

IV. Simulated and Measured Results

The optimized DDF shown in Fig. 1 was fabricated, assembled, and measured. The prototype is shown in Fig. 9. Four polyamide posts were used to maintain the relative vertical distances between the two layers; they ensure the mechanical stability of the filtenna during the measurement process. The impedance measurements were carried out using a Keysight Technologies E5080B four-port vector network analyzer. The far-field characteristics of the prototype were measured in an anechoic chamber. Moreover, a GHC-180-010124 180° hybrid coupler that operates from 1 to 12.4 GHz was adopted to provide both the DM and CM excitations for the measurements.

Fig. 10 provides the measured and simulated S-parameters of the optimized DDF with the DM excitations, and gives the $|S_{11}|$ values of the corresponding theoretical responses. Two resonances (poles) are clearly seen in both operational bands. The measured –10-dB fractional impedance bandwidths (FBWs) are 2.4% (2.42–2.48 GHz) for the lower passband, and 5.2% (5.65–5.95 GHz) for the upper passband. The isolation level between the two differential ports is higher than 36 dB in the lower passband, and is higher than 27 dB in

the upper passband. The measured DM S-parameter results are in good agreement with their simulated and theoretical responses.

Note that the bandwidth of the lower passband was expanded to completely cover the 2.4G WLAN band (2.4–2.484 GHz) in the final tuning process. By increasing the length of the H-shaped slot on the ground plane, one could increase the coupling between the lower frequency CLL and the TM_{10} mode of the patch in order to separate their resonance points in the lower passband. Additionally, a good impedance matching was achieved by adjusting both the coupling strength between the differential feedline and the lower CLL and the height between the two substrates.

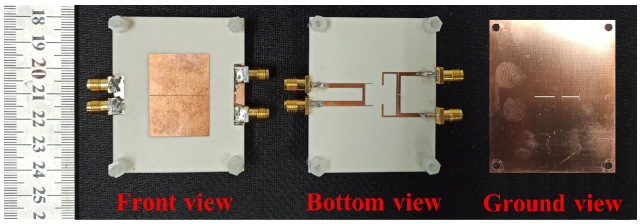

Fig. 9. Photographs of the fabricated DDF.

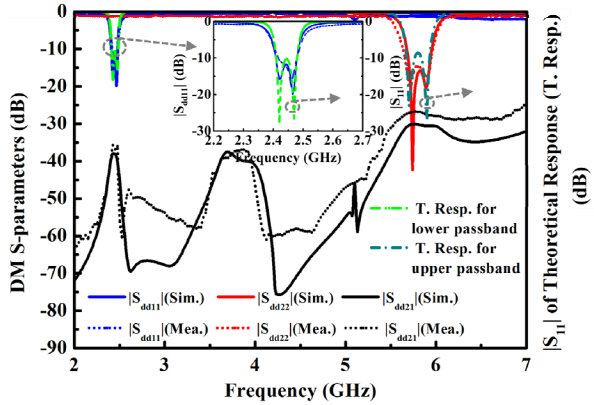

Fig. 10. The measured and simulated S-parameters of the optimized DDF with the DM excitations as functions of the source frequency.

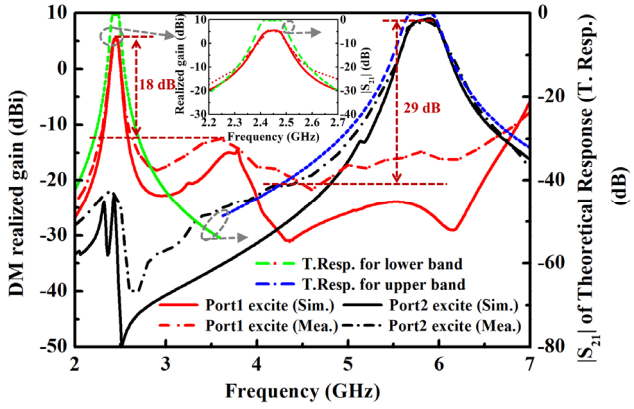

Fig. 11. The measured and simulated realized gain values of the optimized DDF with the DM excitation as functions of the source frequency.

Fig. 11 shows the measured and simulated DM realized gain values of the optimized DDF along with the theoretical $|S_{21}|$ values. It is seen that the realized gain curves associated with each frequency band exhibit a second-order filtering response as designed. The gain curves are flat within the passband and exhibit good lower and upper band-edge selectivity for the lower and higher passbands: 106 dB/GHz, 90 dB/GHz, and 32 dB/GHz, 30 dB/GHz, respectively. When the differential Port 1 is excited, the measured maximum in-band broadside gain and the out-of-band rejection levels are 5.45 dBi at 2.45 GHz and 18.0 dB at 3.6 GHz, respectively. Likewise, when the differential Port 2 is excited, the measured ones are 8.5 dBi at 5.85 GHz and 29.0 dB at 4.2 GHz, respectively. The very minor discrepancies between the measured and simulated values were found with several simulation studies to be mainly due to the various fabrication and assembly tolerances and normal testing errors.

Fig. 12 shows the measured and simulated normalized realized gain patterns at 2.45 GHz and 5.8 GHz. They clearly show that the peak values are in the broadside direction and that the patterns are quite symmetrical with respect to it. The measured co-polarized fields in both the *E*- and *H*-planes are 27 dB larger than the cross-polarized ones at 2.45 GHz and 32 dB larger at 5.8 GHz. These outcomes clearly demonstrate that the optimized DDF with the DM excitations attained high polarization purity in both of its bands.

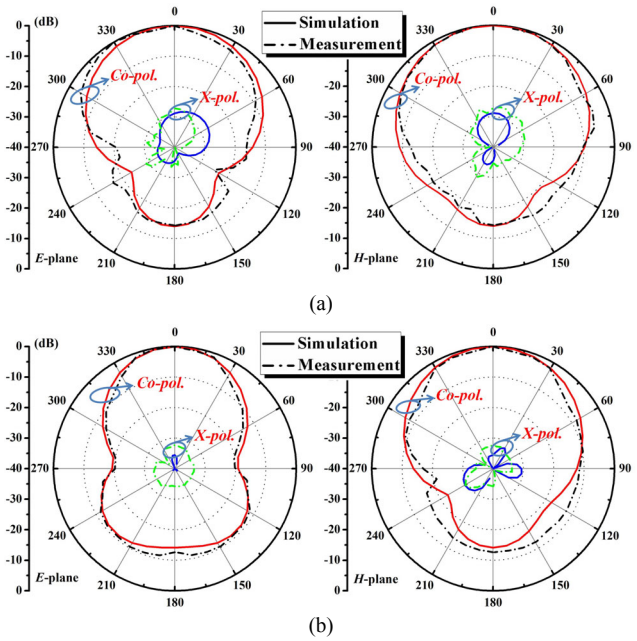

Fig. 12. The measured and simulated normalized realized gain patterns of the optimized DDF with the DM excitations. (a) 2.45 GHz. (b) 5.8 GHz.

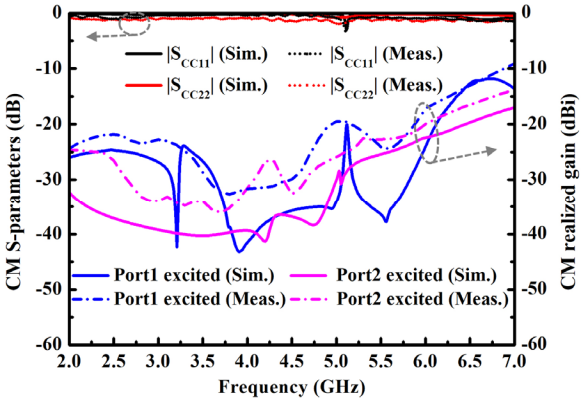

Fig. 13. The measured and simulated S-parameters and realized gains of the developed DDF under CM excitation.

Fig. 13 presents the measured and simulated S-parameters and realized gain values as functions of the source frequency when the DDF is CM excited for comparison purposes. The CM S-parameters ($|S_{cc11}|$ and $|S_{cc22}|$) are essentially 0 dB within the DM passband ranges. Moreover, the measured CM realized gain values are 27 dB and 30 dB lower than the DM realized gain ones within the DM lower and upper passband ranges, respectively. These results clearly demonstrate that the DM excited DDF achieves a very significant, high level of CM suppression.

TABLE II. COMPARISONS OF THE PERFORMANCE CHARACTERISTICS OF THE DDF PROTOTYPE WITH RELATED ANTENNAS REPORTED IN THE LITERATURE

Refs.	FR, IS (*dB*)	Vol. (λ_0^3)	FBW (%)	Peak Real. gain (*dBi*)	Cross-pol. level (*dB*)	SV (dB /GHz)	Diff. feed
[8]	1.06, 29	0.034	1.3 / 1.5	5.8 / 6	28 / 24	N.A.	No
[9]	1.1, 29	0.016	4.5 / 3.6	2.65 / 2.7	22 / 17	85/68 57/40	No
[10]	1.2, 23	0.032	3.2 / 3.9	4.36 / 4.8	34 / 33	85/94 49/75	No
[11]	1.26, 45	0.038	10.6 / 6.9	5.4 / 4.2	18 / 20	142/170 85/57	No
[12]	1.22, 30	0.015	5.9 / 5.8	6.5 / 7	25 / 15	68/43 68/45	No
[13]	2.08, 32	0.003	N.A.	-1.5 / -2.5	8 / 18	N.A.	No
[14]	2.15, 21	0.034	5.3 / 5.7	2.3 / 3.6	28 / 24	40/57 28/31	No
Our work	2.37, 27	0.003	2.4 / 5.2	5.45 / 8.5	27 / 32	106/90 32/30	Yes

* λ_0 is the free space wavelength corresponding to the center frequency, f_0, of the operational band. IS: Isolation. SV: Selectivity value. The SV is calculated as $(R_{max}\text{-}R_{min})/|f_{max}\text{-}f_{min}|$, where R_{max} is the maximum depth of the realized gain null relative to its peak value or is 20 dB if there is no identifiable null. The term R_{min} is simply 3 dB (below the peak value). These realized gain values occur at the frequency points: f_{max} and f_{min}.

Table II provides direct comparisons of the optimized DDF prototype with recently reported, related diplex filtennas. Since our system was based on the TM_{10} and sidelobe-suppressed TM_{30} modes of the patch radiator, a higher FR (larger than 2) value and a smaller volume were achieved simultaneously while maintaining high realized gain values and comparable passband selectivity in comparison to the systems in [8]-[12]. Moreover, in comparison with the single-feed diplex filtennas reported in [8]-[14], our DM-fed system significantly reduces the interconnection losses and fabrication costs in any application involving differential circuits or systems. As a consequence, the integration density of a RF-front end would be further improved with our system. Furthermore, it also achieves a low cross-polarization level and realizes high CM rejection levels. Even with a higher FR, our design realized significantly larger peak realized gain values in both passbands when compared to those in [13], [14]. In particular, since there is no direct cascaded diplexer as in [13] nor the dual slots etched on the radiation side of the patch as in [14], our system avoids the gain reductions witnessed in those works while maintaining a comparable passband selectivity.

V. CONCLUSION

A compact DDF with high CM suppression was reported. The design used a rectangular dual-mode patch resonating in its TM_{10} mode over its lower passband and a TM_{30} mode with a reshaped radiation pattern over its upper passband. Two half-wavelength CLL resonators working at different frequencies were combined with the dual-mode patch. They enhanced the operating bandwidth and provided a second-order Chebyshev filter response over both passbands. An attractive FR value was achieved. The measured results were in very good agreement with their simulated values. With its attractive features including a compact size, high CM noise immunity, low cross-polarization levels, and stable realized gain performance over both of its passbands, the developed DDF system has many potential applications in space-limited, highly integrated RF front-end wireless communication systems.

REFERENCES

[1] Y. M. Pan, P. F. Hu, X. Y. Zhang, and S. Y. Zheng, "A low-profile high gain and wideband filtering antenna with metasurface," *IEEE Trans. Antennas Propag*., vol. 64, no. 5, pp. 2010–2016, May 2016.

[2] C.-X. Mao, S. Gao, Y. Wang, F. Qin, and Q.-X. Chu, "Multimode resonator-fed dual-polarized antenna array with enhanced bandwidth and selectivity," *IEEE Trans. Antennas Propag*., vol. 63, no. 12, pp. 5492–5499, Dec. 2015.

[3] W. Wang, X. Liu, Y. Wu, and Y. Liu, "A broadband filtering patch antenna using T-probe, transverse stubs, and U-Slots," *IEEE Access*, vol. 7, pp. 7502–7509, 2019.

[4] W. Duan, X. Y. Zhang, Y.-M. Pan, J. X. Xu, and Q. Xue, "Dual-Polarized Filtering Antenna With High Selectivity and Low Cross Polarization," *IEEE Trans. Antennas Propag.*, vol. 64, no. 10, pp. 3383–3388, Oct. 2016.

[5] K. Xu, J. Shi, X. Qing, and Z. N. Chen, "A substrate integrated cavity backed filtering slot antenna stacked with a patch for frequency selectivity enhancement," *IEEE Antennas Wireless Propag. Lett*., vol. 17, no. 10, pp. 1910–1914, Oct. 2018.

[6] H.-T. Hu, F.-C. Chen, J.-F. Qian, and Q.-X. Chu, "A differential filtering microstrip antenna array with intrinsic common-mode rejection," *IEEE Trans. Antennas Propag.*, vol. 65, no. 12, pp. 7361–7365, Dec. 2017.

[7] Z.-C. Zhang, S.-W. Wong, J.-Y. Lin, H. Liu, L. Zhu, and Y. He, "Design of multistate diplexers on uniform- and stepped-impedance stub-loaded resonators," *IEEE Trans. Microw. Theory Techn*., vol. 67, no. 4, pp. 1452–1460, Apr. 2019.

[8] A. A. Khan, and M. K. Mandal, "Compact self-diplex antenna using dual-mode SIW square cavity," *IEEE Antennas Wireless Propag. Lett*., vol. 18, no. 2, pp. 343–347, Feb. 2019.

[9] K. Dhwaj, X. Li, L. J. Jiang, and T. Itoh, "Low profile diplex filter/antenna based on common radiating cavity with quasi-elliptic response," *IEEE Antennas Wireless Propag. Lett*., vol. 17, no. 10, pp. 1783–1787, Oct. 2018.

[10] K.-Z. Hu, M.-C. Tang, Y. Wang, and M. Li, "Compact, vertically integrated duplex filtenna with common feeding and radiating SIW cavities," *IEEE Trans. Antennas Propag*., vol. 29, no. 1, pp. 502–507, Jan. 2021.

[11] C.-X. Mao, S. Gao, Y. Wang, Y. Liu, X.-X. Yang, Z.-Q. Cheng, and Y.-L. Geng, "Integrated dual-band filtering/duplexing antennas," *IEEE Access*, vol. 6, pp. 8403–8411, Mar. 2018.

[12] X.-J. Lin, Z.-M. Xie, P.-S. Zhang, and Y. Zhang, "A broadband filtering duplex patch antenna with high isolation," *IEEE Antennas Wireless Propag. Lett*., vol. 16, pp. 1937–1940, 2017.

[13] D. Zayniyev, H. F. AbuTarboush, and D. Budimir, "Microstrip antenna diplexers for wireless communications," in *Proc. Eur. Microw. Conf*., Rome, Italy, Sep. 29–Oct. 1 2009, pp. 1508–1510.

[14] Y.-J. Lee, J.-H. Tarng, and S.-H. Chung, "A filtering diplex antenna for dual-band operation with similar radiation patterns and low cross-polarization levels," *IEEE Antennas Wireless Propag. Lett*., vol. 16, pp. 58–61, 2017.

[15] H. Tang, C. Tang, and J.-X. Chen, "Differential Dual-Polarized Filtering Dielectric Resonator Antenna," *IEEE Trans. Antennas Propag.,* vol. 66, no. 8, pp. 4298–4302, Aug. 2015.

[16] Y. P. Zhang and J. J. Wang, "Theory and analysis of differentially-driven microstrip antennas", *IEEE Trans. Antennas Propag*., vol. 54, no. 4, pp. 1092–1099, Apr. 2006.

[17] L.-H. Zhou and J.-X. Chen, "Differential dual-band filters with flexible frequency ratio using asymmetrical shunt branches for wideband CM suppression," *IEEE Trans. Microw. Theory Techn*., vol. 65, no. 11, pp. 4606–4615, Nov. 2017.

[18] J.-S. Hong and M. J. Lancaster, *Microstrip Filters for RF/Microwave Applications*. New York, NY, USA: Wiley, 2001.

[19] Y.-J. Lu, S.-Y. Chen, and P. Hsu, "A differential-mode wideband bandpass filter with enhanced common-mode suppression using slotline resonator," *IEEE Microw. Wireless Compon. Lett.*, vol. 22, no. 10, pp. 503–505, Oct. 2012.

[20] N.-W. Liu, L. Zhu, W.-W. Choi, and X. Zhang, "Wideband shorted patch antenna under radiation of dual-resonant modes," *IEEE Trans. Antennas Propag*., vol. 65, no. 6, pp. 2789–2796, Jun. 2017.